Investigating the lateral dose response functions of point detectors in proton beams

Kretschmer, Jana; Brodbek, Leonie; Looe, Hui Khee; van der Graaf, Emiel R; van Goethem, Marc-Jan; Kiewiet, Harry; Olivari, Francesco; Meyer, Christoph; Poppe, Bjoern; Brandenburg, Sytze

Published in:
Physics in Medicine and Biology

DOI:
10.1088/1361-6560/ac783c

Physics in Medicine & Biology

ACCEPTED MANUSCRIPT • OPEN ACCESS

Investigating the lateral dose response functions of point detectors in proton beams

To cite this article before publication: Jana Kretschmer *et al* 2022 *Phys. Med. Biol.* in press https://doi.org/10.1088/1361-6560/ac783c

Investigating the lateral dose response functions of point detectors in proton beams

Jana Kretschmer[1,2], Leonie Brodbek[1,2,3], Hui Khee Looe[1], Emiel van der Graaf[2,4], Marc Jan van Goethem[2,4], Harry Kiewiet[4], Francesco Olivari[2], Christoph Meyer[2], Björn Poppe[1], Sytze Brandenburg[2,4]

1) University Clinic for Medical Radiation Physics, Medical Campus Pius Hospital, Carl-von-Ossietzky University Oldenburg, Germany

2) Department of Radiation Oncology, University Medical Center Groningen, University of Groningen, The Netherlands

3) EBG MedAustron GmbH, Marie Curie-Straße 5, A-2700, Wiener Neustadt, Austria

4) Particle Therapy Research Center, University Medical Center Groningen, University of Groningen, The Netherlands

Abstract

Objective

Point detector measurements in proton fields are perturbed by the volume effect originating from geometrical volume-averaging within the extended detector's sensitive volume and density perturbations by non-water equivalent detector components. Detector specific lateral dose response functions $K(x)$ can be used to characterize the volume effect within the framework of a mathematical convolution model, where $K(x)$ is the convolution kernel transforming the true dose profile $D(x)$ into the measured signal profile of a detector $M(x)$. The aim of this work is to investigate $K(x)$ for detectors in proton beams.

Approach

The $K(x)$ for five detectors were determined by iterative deconvolution of measurements of $D(x)$ and $M(x)$ profiles at 2 cm water equivalent depth of a narrow 150 MeV proton beam. Monte Carlo simulations were carried out for two selected detectors to investigate a potential energy dependence, and to study the contribution of volume-averaging and density perturbation to the volume effect.

Main results

The Monte Carlo simulated and experimentally determined $K(x)$ agree within 2.1% of the maximum value. Further simulations demonstrate that the main contribution to the volume effect is volume-averaging. The results indicate that an energy or depth dependence of $K(x)$ is almost negligible in proton beams. While the signal reduction from a Semiflex 3D ionization chamber in the center of a gaussian shaped field with 2 mm sigma is 32% for photons, it is 15% for protons. When measuring the field with a microDiamond the trend is less pronounced and reversed with a signal reduction for protons of 3.9% and photons of 1.9%.

Significance

The determined $K(x)$ can be applied to characterize the influence of the volume effect on detectors measured signal profiles at all clinical proton energies and measurement depths. The functions can be used to derive the actual dose distribution from point detector measurements.

1 Introduction

While modern proton pencil beam scanning (PBS) with almost vanishing dose at positions beyond the Bragg-peak allows for effective sparing of healthy tissue in beam direction, the lateral dose fall-off (penumbra) of such intensity-modulated proton beams is limited by the penumbra of the single pencil beams. In the past few years, irradiation techniques have been investigated and implemented, which aim to steepen the lateral penumbra of proton beams to better spare adjacent organs-at-risk or to better conform the radiation beam to small lesions. These techniques comprise PBS in combination with collimating apertures or a dynamic collimation system, PBS with a reduced air gap between nozzle and patient, or combined with edge-enhanced collimation (Hyer et al., 2014; Winterhalter et al., 2018; Ciocca et al., 2019; Grevillot et al., 2020).

For general PBS with gaussian shaped pencil beams, previous studies indicate that the volume effect of detectors, which comprises the volume-averaging and density effects, does not or only slightly influence the measurement process (Brodbek et al., 2020; Furukawa et al., 2013; Moignier et al., 2017; Sahoo et al., 2010; Schwaab et al., 2011). In contrast, insight into the performance of point detectors in proton beams with reduced penumbrae is scarce. While McAuley et al. (2015) found no significant difference between the profiles of a scattered collimated proton beam measured with high resolution film and a diode detector, Hoehr et al. (2018) identified differences in output factor measurements for collimated 74 MeV scattered proton fields down to 5 mm diameter measured with a diode detector. Lomax (2018) predicts that developments in proton therapy comprise a trend towards reduced penumbras and (very) small field dosimetry. For both steep penumbras and small fields, i.e. wherever the spatial dose distribution exhibits strongly varying gradients, special care must be taken to mitigate perturbations due to the volume effect of point detectors.

Describing the measurement process with a convolution model, the volume effect of a detector can be characterized by its lateral dose response function *K*(*x,y*) that encompasses two contributing mechanisms: the volume-averaging within the extended sensitive volume and the density perturbation that results from the disturbance of the charged particle fluence by non-water-equivalent detector components (Looe et al., 2013, 2015; Poppinga et al., 2015). The function *K*(*x,y*) acts as the convolution kernel transforming the undisturbed dose distribution *D*(*x,y*) into the measured signal distribution *M*(*x,y*) (Looe et al., 2013; Harder et al., 2014; Looe et al., 2015, 2015; Poppinga et al., 2015; Looe et al., 2017; Brodbek et al., 2020):

$$M(x,y) = K(x,y) * D(x,y) = \int_{-\infty}^{\infty}\int_{-\infty}^{\infty} K(x-u,y-v)D(u,v)\,du\,dv \quad (1)$$

When *K*(*x,y*) is known for a certain detector, the dose profiles *D*(*x,y*) can be recovered from the measured profiles *M*(*x,y*) by deconvolution (Laub and Wong, 2003). *K*(*x,y*) for photon fields have been derived experimentally and/or by Monte Carlo simulations (Gago-Arias et al., 2012; Looe et al., 2013, 2015; Poppinga et al., 2015; Looe et al., 2017; Delfs et al., 2018). To do so, *D*(*x,y*) and *M*(*x,y*) profiles of a narrow slit beam or pencil beam were obtained such that *K*(*x,y*) could be derived from the relationship in Equation 1 for a large set of detectors (Gago-Arias et al., 2012; Looe et al., 2013; Poppinga et al., 2015; Looe et al., 2015, 2017; Delfs et al., 2018). Considering the shorter average secondary electron range in proton beams as compared to photons (Brodbek et al. 2020) the influence of the density perturbation is anticipated to be smaller in proton beams, while the volume-averaging component remains the same. Therefore, the lateral dose response functions of detectors for proton beams are expected to differ from that for photon beams and to the best of our knowledge have not yet been studied.

The aim of this work is to experimentally determine one-dimensional *K*(*x*) of a number of detectors in proton beams, that can be transformed to two-dimensional functions by considering the detectors' rotational symmetry. The lateral profiles *D*(*x*) and *M*(*x*) of a scattered 150 MeV proton beam collimated by a 0.5 mm wide slit collimator were measured at 2 cm water equivalent depth with EBT3 film and point detectors, respectively. Using the previously described convolution model (Equation 1), *K*(*x*) was determined for three ionization chambers, a silicon diode and a diamond detector. The depth dependence of *K*(*x*) was investigated by applying the *K(x)* derived at 2 cm depth to profiles measured at larger depths. In addition, Monte Carlo simulations to elucidate the contributions of volume-averaging and density perturbation to the total volume effect of the detectors in clinical proton beams were performed and simulations for 60 MeV and 240 MeV protons were used to study a potential energy dependence.

2 Method

2.1 Determination of *K*(*x*)

2.1.1 Setup

Experiments were performed at the PARTREC Accelerator Facility (University Medical Center Groningen, University of Groningen) using a dedicated narrow proton beam geometry. A 150 MeV proton beam was scattered by a 1.44 mm Pb foil, located 3.03 m upstream from a 50 mm diameter, 45 mm thick circular brass collimator. Prior to the actual measurements the flatness of the 50 mm diameter field was checked using a CCD/scintillator system (scintillator: Kodak LANEX Fine®; camera: Apogee ALTA® E1, CCD: Kodak Blue Plus® full frame sensor; 768x512 pixels of 9x9 μm^2). Subsequently the proton beam was further collimated to create the desired narrow beam profile. Preliminary experiments showed that the narrow dose distribution needed to derive *K(x)* can be obtained by using a 104 mm thick slit collimator and a slit width of 0.5 mm. During the experiments, the slit collimator was placed at approximately 3.1 m from the scatter foil on a translation (Newport M-443) and rotation stage (Newport URS 100BC) to align the slit collimator with the beam by optimizing the slit output at the center and the symmetry of the measured profile.

2.1.2 Dose profiles *D*(*x*)

The *D*(*x*) profiles of the slit beam were measured with Gafchromic EBT3 films in a 250 mm (*x*) x 258 mm (*y*) x 554 mm (*z*) water phantom with a 2.9 mm thick polycarbonate entrance window located 43 mm from the slit collimator exit. The film response was calibrated in a 50 mm diameter 150 MeV proton beam against the dose measured with a PTW Markus chamber type 23343 (0, 0.02, 0.05, 0.1, 0.21, 0.42, 0.84, 1.1, 1.7 and 4.2 Gy) at 2 cm depth in a polystyrene phantom. The calibration was performed following the procedure described in Brodbek et al. (2020) but using two third-degree polynomial fit functions, one for the low and another for the high dose range, to improve the goodness of the fit over the entire dose range. To warrant an overall smooth calibration curve the two ranges had an overlap of three measurement points. Using the calibrated films *D*(*x*) profiles were acquired at 2 cm, 8 cm and 13 cm water equivalent depth at corresponding residual ranges of approximately 12.2 cm, 6.2 cm and 1.2 cm. The films were scanned with an Epson 10000XL flatbed scanner (Seiko Epson Corp., Suwa, Japan) at a resolution of 600 dpi and 48 bit. The *D*(*x*) profile of each film was obtained from the average of 71 pixel rows (3 mm) across the measured profile. For each individual film, the background was estimated by averaging the dose in 3x3 mm^2 regions in the four corners of the film (see section 4.2). The *D*(*x*) profiles were determined as the mean of three independent background-corrected film measurements.

2.1.3 Signal profiles *M(x)*

The corresponding *M(x)* profiles were acquired using three ionization chambers (a Semiflex 3D 31021 and a PinPoint 3D 31022 from PTW Freiburg, Germany and a CC01G Razor chamber from IBA Dosimetry, Schwarzenbruck, Germany), as well as a microSilicon diode 60023 and a microDiamond detector 60019 (both from PTW Freiburg, Germany). Geometrical information on the sensitive volumes of all five investigated detectors is given in table 1. All detectors were positioned with the detector axis parallel to the beam axis. *M*(*x*) profiles were acquired at 2 cm, 8 cm and 13 cm water equivalent depth taking into account the effective points of measurement. The detector signal was read out with an UNIDOS electrometer type 10001 (PTW Freiburg, Germany) as a function of lateral position across the profile in the water phantom. The detectors were moved using a translation stage (Thorlabs NRT100/M) with 0.015 mm accuracy and variable step sizes (between 0.1 mm and 0.5 mm) chosen according to the profile shape and dose gradient. A fixed number of Monitor Units (MU) was delivered for all points in one profile.

Table 1: Diameters of the detectors including wall material and of the detectors sensitive area for all investigated point detectors as well as the sensitive detector volumes in mm^3 as calculated from finite-element methods taken from (Tekin et al., 2020) (*) or calculated using data given in (Tekin et al., 2022) (**).

Detector	Outer detector diameter in mm	Diameter of sensitive area in mm	Sensitive volume in mm^3
microSilicon 60023 (PTW)	6.9	1.5	0.03(*)

microDiamond 60019 (PTW)	6.9	2.2	0.004(*)
CC01G Razor (IBA)	3.0	2.0	9.185
PinPoint 3D 31022 (PTW)	4.3	2.9	13.1(**)
Semiflex 3D 31021 (PTW)	6.1	4.8	52.5(**)

The detector specific $K(x)$ were derived according to Equation 1 from the measured $D(x)$ and $M(x)$ using the iterative van Cittert (1931) deconvolution method as described in Looe et al. (2015). The number of iterations was limited to five to suppress the unavoidable noise amplification during the iteration process. Prior to deconvolution, the measured $M(x)$ and $D(x)$ were pre-processed by first interpolating them using a cubic spline interpolation in MATLAB R2019b (MATLAB, 2019) and subsequently taking the average of the left- and right side of the profiles.

2.2 Monte Carlo simulations

Validation of *K(x)* by Monte Carlo simulations

Monte Carlo simulations in GATEV9.0/Geant4.10.06.p03 were performed to further investigate the experimentally determined $K(x)$. The complete beam line model of the PARTREC Irradiation Facility as described by Mulder (2017) was implemented and adapted to correspond to the actual setup described in section 2.1. The simulations are performed completely independent from the measurements. In the first step, a proton phase space file was generated directly behind the exit plane of the slit collimator using the *PhaseSpaceActor*. Subsequently, the $D(x)$ profile was scored at 2 cm depth in a water phantom using a 0.1 mm (x) x 20 mm (y) x 0.1 mm (z) water voxel. $M(x)$ profiles of the Semiflex 3D chamber and microDiamond were simulated at the same depth using a step size of 0.1 mm within the central area of the slit beam and a step size of 0.5 mm in the outer region. Detailed models of the detectors were built based on constructional drawings provided by the manufacturers. Figure 1 shows the geometry details and material information of the two detectors as implemented in the Monte Carlo code. The sensitive volume of the Semiflex 3D chamber derived using finite-element methods as described in Delfs et al. (2021) was implemented. In addition to the 150 MeV protons as used during the experiments, the simulations were also done for incident proton energies of 60 MeV and 240 MeV.

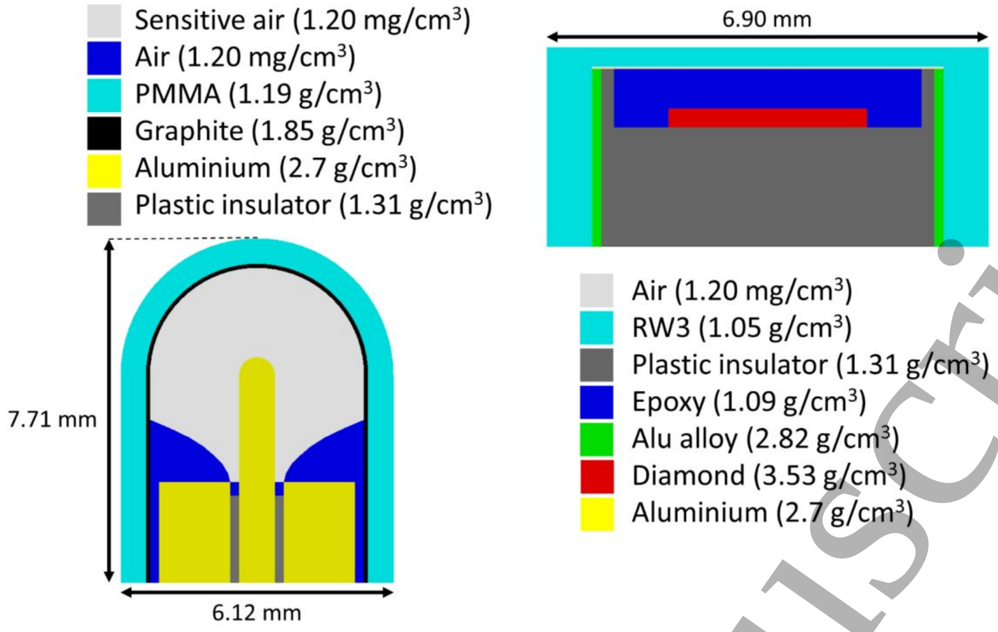

Figure 1: Geometries (not true to scale) and materials with density given in parenthesis of the PTW Semiflex 3D 31021 chamber (left, material information above) and the microDiamond 60019 detector (right, material information below) as implemented in the Monte Carlo code GATE. The air and aluminum part of the microDiamond below the RW3 layer are too thin to be visible.

Contribution of the volume-averaging and the density perturbation

To investigate the contribution of the volume-averaging and the density perturbation on the detector's volume effect in proton beams, *K(x)* were determined from *M(x)* simulations performed as described above using a modified detector geometry instead of the complete detector models. In the first modification, $M_{sens}(x)$ profiles were simulated by replacing all detector components with water, except the sensitive volume. By comparing $M_{sens}(x)$ and $M(x)$ the perturbation caused by the presence of the non-water equivalent components surrounding the sensitive volume was established. In a second step, all detector component materials, including the sensitive detector volume, were replaced by water to obtain the profiles $M_{water}(x)$ representing the contribution from only the volume-averaging.

Monte Carlo simulation settings

The physics parameters in GATE/Geant4 used in this work were selected based on previous publications (Wulff et al., 2018; Simiele and DeWerd, 2018; Kretschmer et al., 2020). The settings are summarized in the table S1 provided as supplementary material following the

Monte Carlo reporting recommendations by Sechopoulos et al. (2018). The stopping power tables for G4_AIR and G4_WATER based on the ICRU Report 90 (Seltzer et al., 2016) were used for the simulations by setting the corresponding command in GATE (/gate/physics/setUseICRU90DataFlag true). The mean excitation energy of graphite used was 81 eV, in agreement with the recent ICRU recommendation (Seltzer et al., 2016).

3 Results

3.1 Measured *D*(*x*) and *M*(*x*)

The experimentally determined *D*(*x*) and *M*(*x*) profiles of the optimized narrow slit beam geometry at 2 cm, 8 cm and 13 cm water equivalent depth with corresponding residual ranges in water of approximately 12.2 cm, 6.2 cm and 1.2 cm are shown in figure 2. Note that all profiles are normalized to their maxima. A constant background of approximately 0.02 Gy was subtracted from the *D*(*x*) profiles, which have peak dose values of at least 1 Gy. Table 5 lists the corresponding FWHM and $d_{80/20}$. The tabulated $d_{80/20}$ values were computed as the average $d_{80/20}$ values of the left and right profile sides. At 2 cm depth, all *M*(*x*) profiles have a larger $d_{80/20}$ than the *D*(*x*) profile. While the FWHM of the *D*(*x*) profile is 0.7 mm, the *M*(*x*) profile of the microSilicon and Semiflex 3D have a FWHM of 1.3 mm and 3.9 mm, respectively.

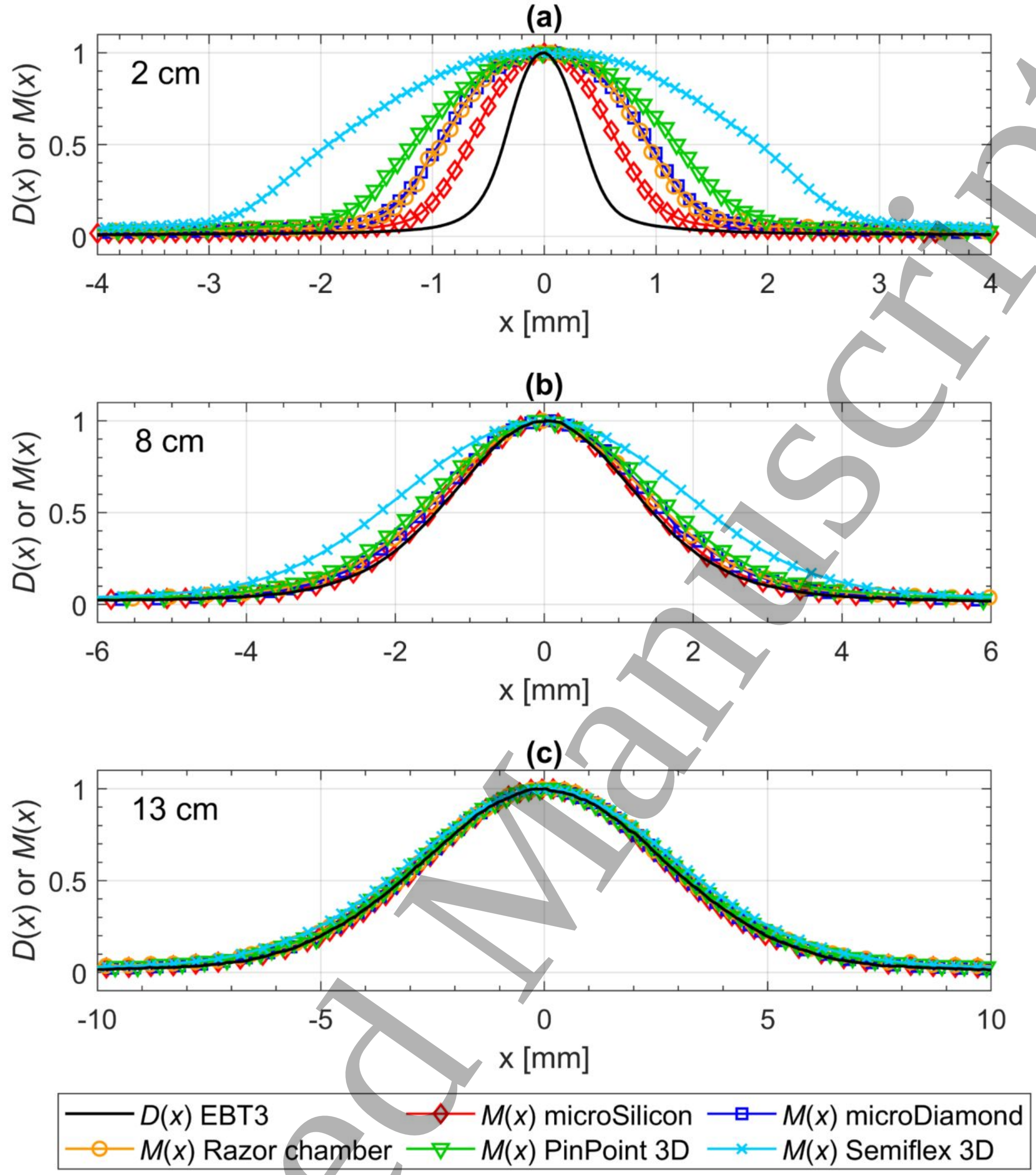

Figure 2: Measured profiles *M*(*x*) in comparison to *D*(*x*) determined with EBT3 film at (a) 2 cm, (b) 8 cm and (c) 13 cm depth in water for all investigated detectors. All profiles have been normalized to their respective maximum. Note the difference in the x-scales.

Table 2: FWHM and $d_{80/20}$ of experimentally determined *D*(*x*) and *M*(*x*) profiles shown in figure 2. The uncertainty of the values is estimated as half the distance between two measurement points, which is 0.02 mm for the *D(x)* profile and 0.05 mm for the *M(x)* profiles.

Depth	2 cm		8 cm		13 cm	
	$d_{80/20}$ [mm]	FWHM [mm]	$d_{80/20}$ [mm]	FWHM [mm]	$d_{80/20}$ [mm]	FWHM [mm]
***D(x)* - Film**	0.35	0.73	1.58	2.92	3.30	6.44
***M(x)* - microSilicon**	0.57	1.34	1.59	3.05	3.19	6.34
***M(x)* - microDiamond**	0.68	1.90	1.68	3.24	3.25	6.45
***M(x)* - Razor chamber**	0.65	1.84	1.70	3.27	3.36	6.49
***M(x)* - PinPoint 3D**	0.87	2.37	1.80	3.50	3.27	6.58
***M(x)* - Semiflex 3D**	1.33	3.86	2.10	4.43	3.51	7.00

3.2 Experimentally determined *K*(*x*)

The *K*(*x*) derived from the 2 cm depth measurements, normalized to their respective maximum are presented in figure 3. Please note that during convolutions, the *K(x)* are area-normalized. All *K*(*x*) show almost vanishing values beyond the borders of the detector's sensitive volume. However small oscillations can be observed at the borders of the detectors, especially for the diode type detectors. The origin of these oscillations will be analyzed in the discussion.

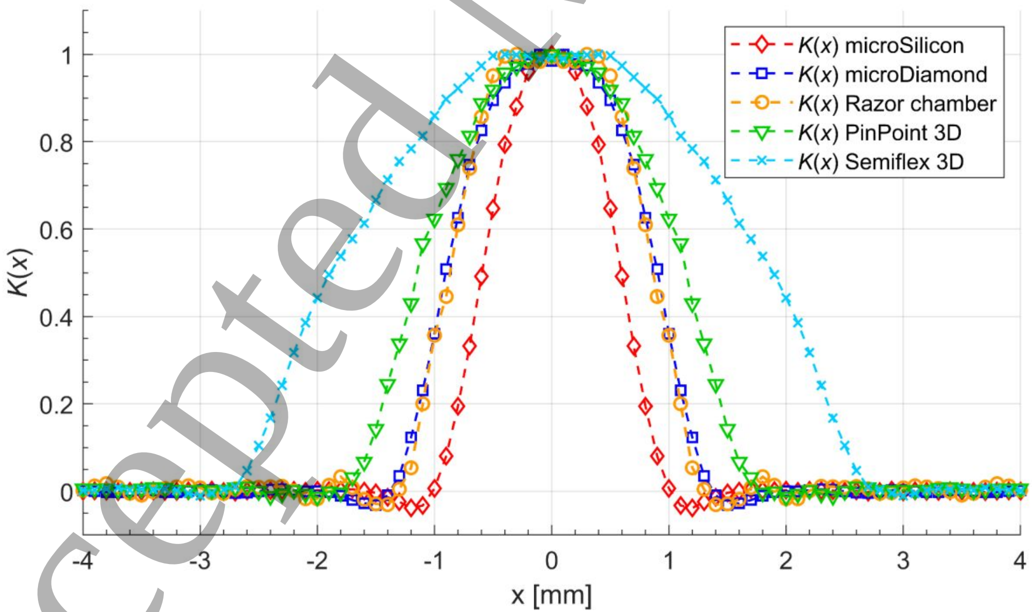

Figure 3: Comparison of experimentally derived lateral dose response functions *K*(*x*) determined based on measurements of *D*(*x*) and *M*(*x*) at 2 cm depth in water. All curves are normalized to their respective maximum.

3.3 Validation of *K*(*x*) at larger depths

To investigate the applicability of the $K(x)$ determined at 2 cm depth at larger measurement depths, the measured $D(x)$ profiles at 8 cm and 13 cm depth were convolved with the $K(x)$ shown in figure 3 ($K_{2cm}(x) * D_{8cm/13cm}(x)$) and compared to actual measurements of $M_{8cm/13cm}(x)$ performed with the Semiflex 3D chamber and microDiamond. The comparison shown in figure 4 reveals that the convolution products $K_{2cm}(x) * D_{8cm/13cm}(x)$ and the measured $M_{8cm/13cm}(x)$ agree well for both measurement depths and detectors.

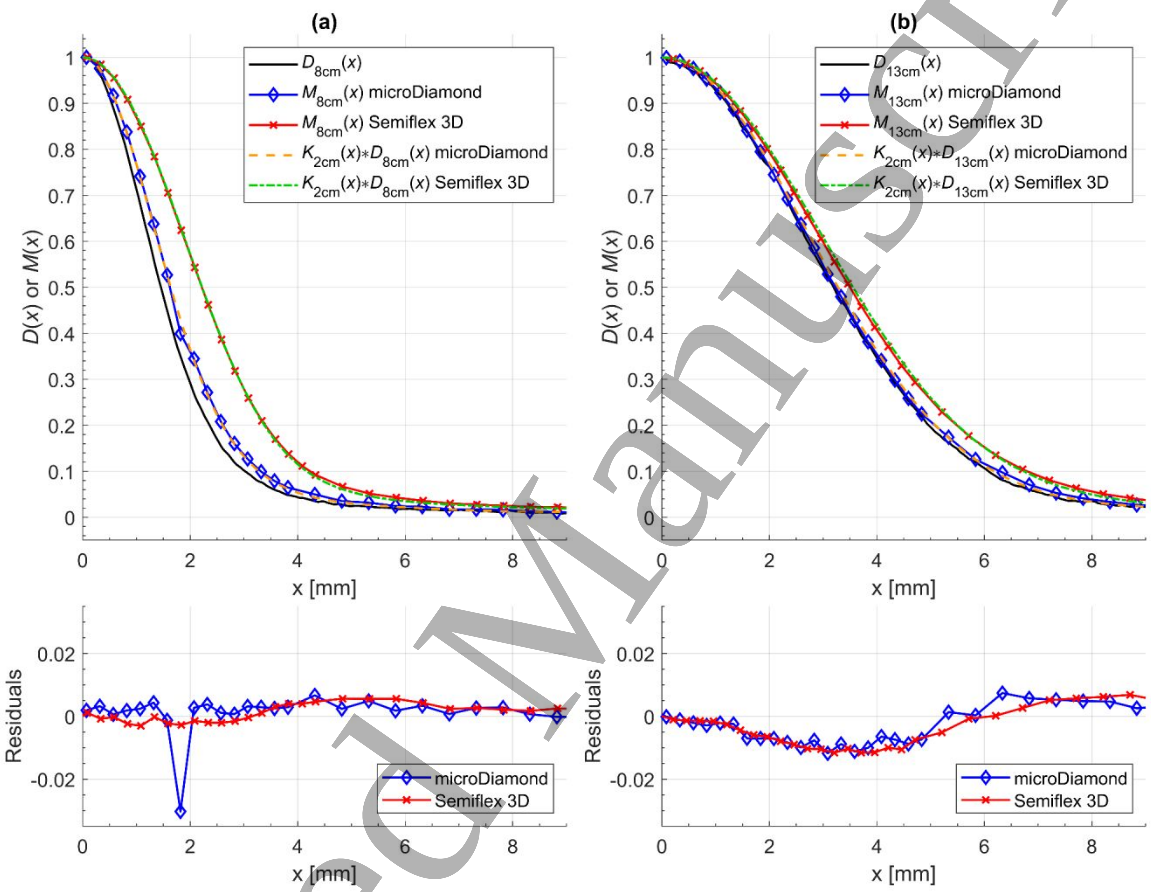

Figure 4: Measured profiles $M_{8cm/13cm}(x)$ in comparison to $K_{2cm}(x) * D_{8cm/13cm}(x)$ for the Semiflex 3D and microDiamond at (a) 8 cm and (b) 13 cm depth in water. All profiles have been normalized to their respective maximum. The residuals represent the difference between the normalized profiles associated with each detector.

3.4 Comparison between experiment and Monte Carlo simulations

Figure 5 shows a comparison of the experimentally and Monte Carlo simulated $K(x)$ derived for the Semiflex 3D and microDiamond using a 150 MeV proton slit beam at 2 cm depth. The comparison reveals that the maximum-normalized $K(x)$ agree within ±0.03 for both detectors. A comparison of the corresponding *D(x)* and *M(x)* profiles is provided as supplementary material (figures S1 and S2).

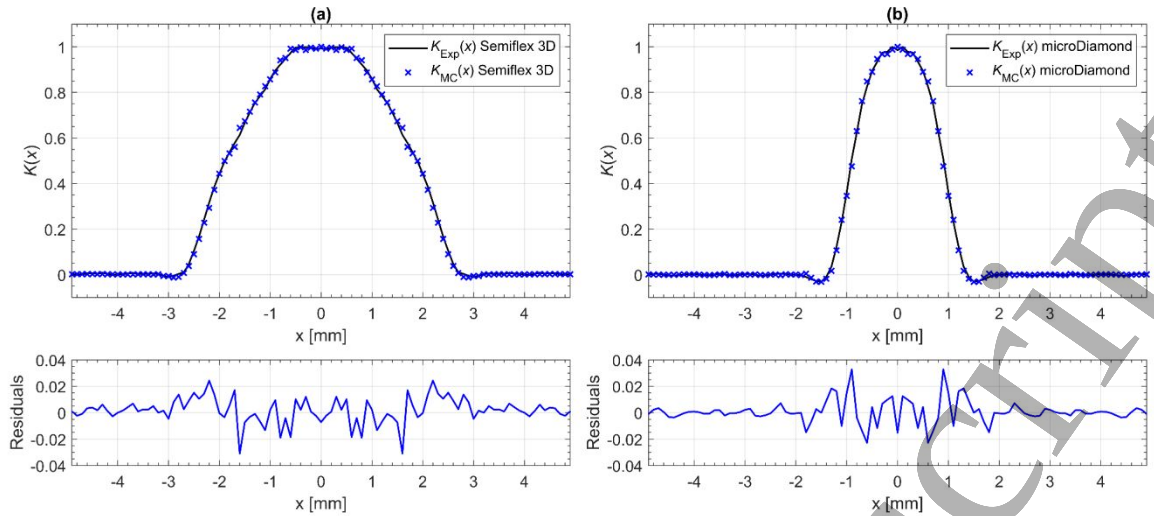

Figure 5: Comparison of the lateral dose response functions $K(x)$ determined experimentally (Exp) and by Monte Carlo simulations (MC) for the Semiflex 3D (a) and microDiamond (b) at 2 cm depth in water. All profiles are normalized to their respective maximum. The residuals represent the difference between the measurement and simulation.

3.5 Influence of detector components on *K(x)*

Figure 6 shows the comparison of $K(x)$, $K_{sens}(x)$ and $K_{water}(x)$ for the Semiflex 3D (a) and microDiamond detector (b). The functions were determined by deconvolution of the $M(x)$, $M_{sens}(x)$ and $M_{water}(x)$, respectively, with $D(x)$. The $M(x)$ profiles were simulated using the modified detector geometries of the Semiflex 3D chamber and the microDiamond detector and are provided as supplementary material (figure S3). For the Semiflex 3D chamber, the $K(x)$ and $K_{sens}(x)$ functions are the same within the uncertainty of the simulations while a 0.2 mm difference in FWHM between $K(x)$ and $K_{water}(x)$ can be observed. In contrast, all three functions associated with the microDiamond detector are the same within the uncertainty of the simulations.

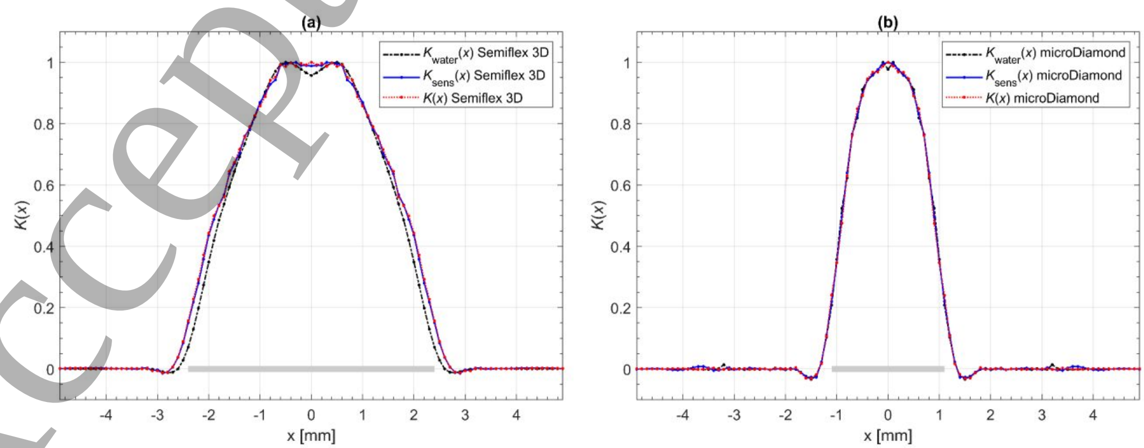

Figure 6: Maximum-normalized lateral dose response functions $K(x)$ for the Semiflex 3D chamber (a) and microDiamond (b) derived from Monte Carlo simulations of *D(x)* and *M(x)* for modified detector geometries. The red line shows the function obtained by modelling the whole detector, the blue line the function resulting if only the sensitive detector volume is implemented in the simulation. The black line shows the function obtained if all detector materials are replaced by water. The grey area indicates the width of the sensitive volume.

3.6 Dependence of *K*(*x*) on incident proton energy

The $K(x)$ functions derived for the Semiflex 3D and microDiamond detector at three different energies are presented in figure 7 (a) and (b). The corresponding simulated *D(x)* and *M(x)* profiles as well as associated FWHM and $d_{80/20}$ are provided as supplementary material (figures S4 and S5, table S2). Both the $K_{150\mathrm{MeV}}(x)$ and $K_{240\mathrm{MeV}}(x)$ are very similar while the $K_{60\mathrm{MeV}}(x)$ shows a penumbra that is less steep.

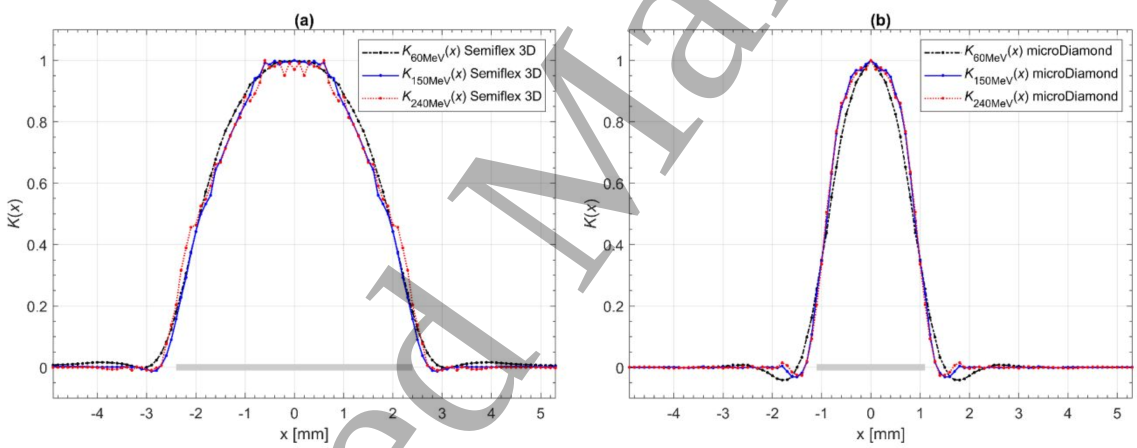

Figure 7: Maximum-normalized lateral dose response functions $K(x)$ for the Semiflex 3D (a) and microDiamond (b) derived from Monte Carlo simulated *D(x)* and *M(x)* at incident proton energies of 60 MeV, 150 MeV and 240 MeV at 2 cm depth in water. The grey area indicates the width of the sensitive volume area.

The clinical significance of this energy dependence observed in the $K(x)$ has been investigated in figure 8 showing a comparison of the convolution of $D(x)$ at 60 MeV and 240 MeV with the simulated $K_{150\mathrm{MeV}}(x)$ and the corresponding signal profiles $M(x)$ obtained at 60 MeV and 240 MeV, respectively. A discussion is provided in section 4.3.

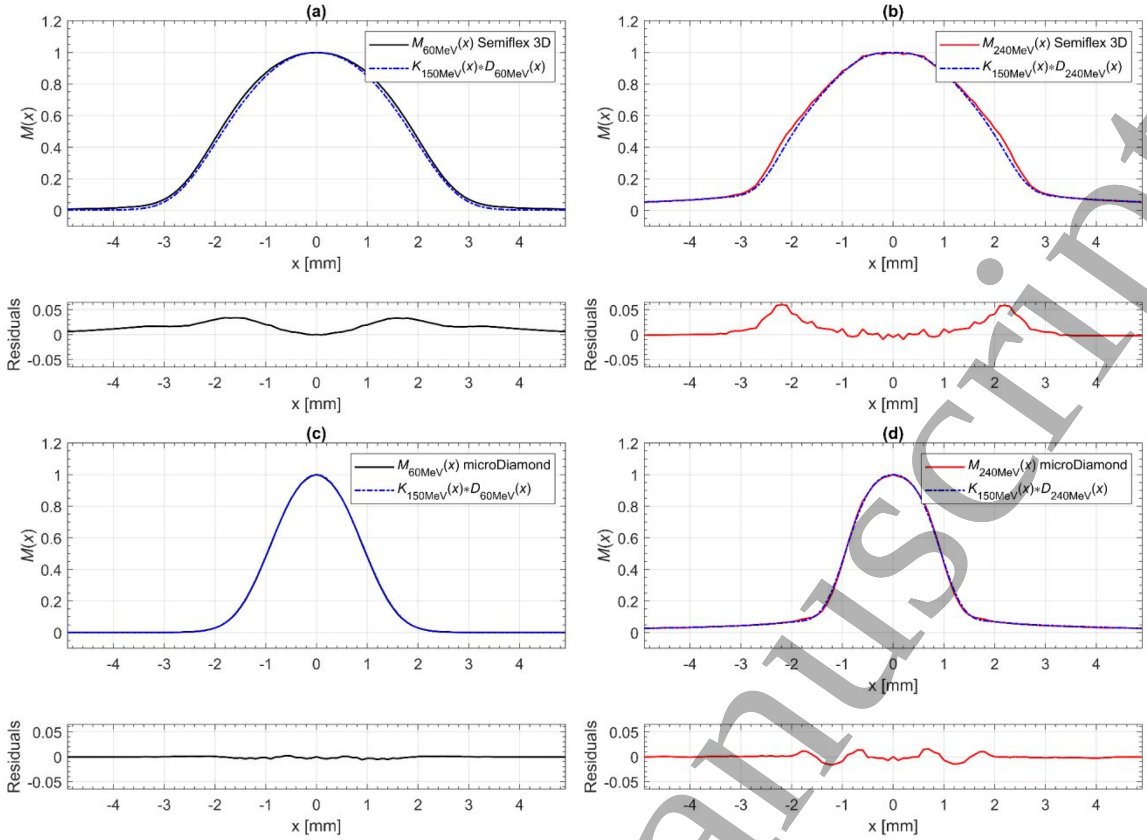

Figure 8: Simulated measured signal profiles $M(x)$ of the Semiflex 3D ((a) and (b)) and microDiamond ((c) and (d)) for 60 MeV and 240 MeV in comparison to the convolutions $K_{150\mathrm{MeV}}(x) * D_{60\mathrm{MeV}}(x)$ ((a) and (c)) and $K_{150\mathrm{MeV}}(x) * D_{240\mathrm{MeV}}(x)$ ((b) and (d)). All profiles have been normalized to their respective maximum. The residuals represent the difference between the normalized profiles.

4 Discussion

4.1 Volume effect in proton beams

Lateral dose response functions $K(x)$ have been experimentally determined for five point detectors at 2 cm depth in water using a 150 MeV proton slit beam. The profiles $M(x)$ measured with various detectors reveal a volume effect for all investigated detectors. The FWHM and $d_{80/20}$ values of both $D(x)$ and $M(x)$ increase with the measurement depth due to beam broadening from multiple coulomb scattering and nuclear interactions. As a result, the differences between the $D(x)$ and $M(x)$ profiles become smaller with the depth.

The residuals of the experimentally and Monte Carlo simulated *K(x)* for the Semiflex 3D chamber and microDiamond agree within 0.03. This good agreement allowed further investigations of the underlying mechanisms of the observed volume effect in proton beams.

Detailed Monte Carlo simulations were performed to separately study the volume-averaging and the density perturbation caused by non-water equivalent detector components.

For the Semiflex 3D chamber, the $K_{water}(x)$ that solely represents the volume-averaging of the chamber is narrower than the $K_{sens}(x)$, where the sensitive volume consists of air. This difference indicates a disturbance of the particle fluence by the air cavity of the chamber due to its much lower density. The same effect has been reported for air-filled chambers in photon fields (Looe et al., 2015) as caused by an increased signal contribution from inward-directed transport of secondary electrons. The difference observed here is much less prominent than in photon fields, which is explained by the much shorter range of the secondary electrons in proton beams causing most of the dose to be deposited close to the track of the primary protons (Brodbek et al., 2020). The presence of not water-equivalent components such as the aluminum central electrode or graphite and PMMA wall does not perturb the measurements as is shown by very small differences between $K_{sens}(x)$ and $K(x)$ (residuals of maximum normalized distributions within 0.02).

As shown in figure 6, the differences between $K(x)$, $K_{sens}(x)$ and $K_{water}(x)$ of the microDiamond detector can be considered negligible (residuals within 0.05). The results show that the thin (in the range of micrometers) sensitive volume of diode-type detectors and their surrounding materials are not causing any significant fluence perturbation. In other words, the volume effect of diode-type detectors can be solely attributed to averaging over sensitive volume of the detector. This agrees with findings by Moignier et al. (2017), who studied diamond detector design and performed Monte Carlo simulations mimicking the measurement process of a 100 MeV proton pencil beam profile. They used a water voxel, diamond voxels of various size (widths between 0.25 mm and 4 mm) and a complete detector geometry. The profiles obtained with the water voxel, with the complete detector and a diamond voxel having the same size as the other two scoring volumes differed by less than 1%. Based on these results, it is noteworthy that detector over-response along the beam's axis and profile steepening at the beam penumbra associated to the density perturbation of diode-type detectors, as frequently reported for photon fields (Francescon et al., 2014; Looe et al., 2015; Poppinga et al., 2015), are expected to be much less prominent in proton beams because of the much lower secondary electron energy.

To estimate the contributions of the geometrical volume-averaging effect and the density perturbation to the overall detector's volume effect and to provide a comparison between photons and protons, calculations based on equation 1 have been performed for a small exemplary field. The results of the investigation are shown in figure 9. As the volume effect is most pronounced in small fields, the dose profile $D(x)$ used for the calculations was created by a gaussian function with a sigma of 2 mm representing the lower limit of the clinical field sizes used in most state-of-the-art delivery techniques. The presented perturbed $M(x)$ profiles were derived by applying equation 1 in the one-dimensional case such that $D(x)$ was convolved with the lateral dose response functions $K(x)$ of the Semiflex 3D chamber and the microDiamond detector as presented in figure 2. Thereby, the contribution from the overall volume effect in protons $M_{\mathrm{proton}}(x) = D(x) * K(x)$ was estimated. For photons, the corresponding $K_{\mathrm{6MV}}(x)$ of both detectors, valid for 6 MV photons, as previously published by Delfs et al. (2018) were used to derive the overall volume effect in photons $M_{\mathrm{photon}}(x) = D(x) * K_{\mathrm{6MV}}(x)$. Additionally, the $K_{\mathrm{water}}(x)$ that characterizes solely the volume-averaging effect in proton fields, which is independent of the beam quality (Looe et al., 2015), were used for both detectors to determine perturbed measured signal profiles resulting from solely the volume-averaging effect $M_{\mathrm{water}}(x) = D(x) * K_{\mathrm{water}}(x)$. For the Semiflex 3D chamber, the comparison shows that a perturbation for the exemplary field would be larger in photons than in protons with corresponding signal reductions at the field center (output) of 32% for photons and 15% for protons. In contrast, the signal reduction with a microDiamond is larger for protons by 3.9% in comparison to a photon field with a reduction of 1.9% as the density perturbation in the latter caused by the higher density detector components results in an overresponse (Looe et al., 2015; Poppinga et al., 2015). The difference between $M_{\mathrm{water}}(0)$ and $M_{\mathrm{proton}}(0)$ that can be attributed to the density perturbation amounts to 2% for the Semiflex 3D and is negligible (0.1%) for the microDiamond.

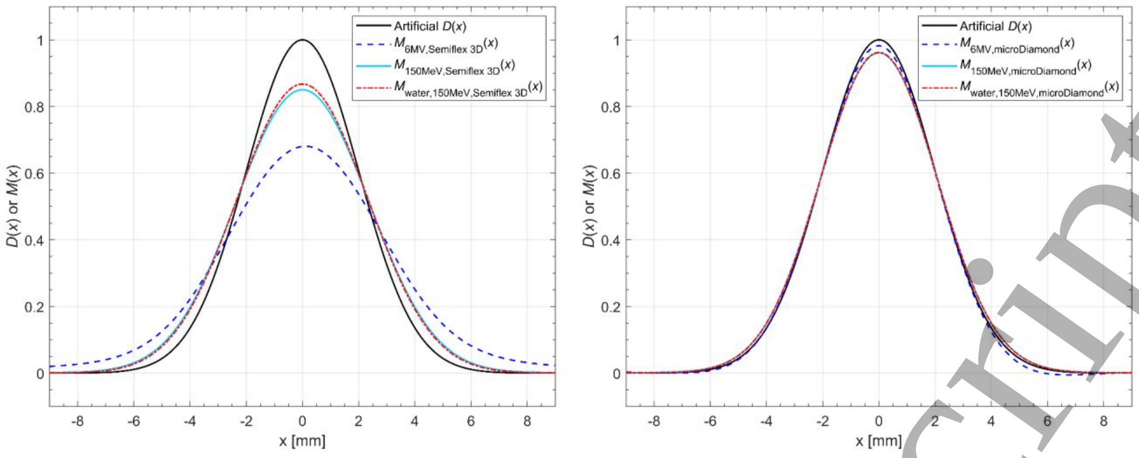

Figure 9: Estimation of the contributions of the geometrical volume-averaging effect and the density perturbation to the overall detector's volume effect as well as a comparison between proton and photon beam for an exemplary small field. See text for details.

The derived $K(x)$ for the diode-type detector show small oscillations at the detector edges. In photon beam dosimetry, the $K(x)$ of diode detectors also exhibit such negative values at the detector borders, which in that case are due to the perturbation of the secondary electron transport by the presence of higher density detector components (Looe et al., 2015). However, the magnitude of these negative values is usually much larger in photon fields than that observed in this work. Furthermore, the $K_{water}(x)$ determined for the microDiamond derived without any detector components also shows the same oscillations. Thus, the oscillations cannot be attributed to the perturbation of the particle fluence by non-water equivalent detector components like in photon beams. Further evidence for this is found in figure 7, which shows that the $K_{60MeV}(x)$ calculated from the lowest energy simulations exhibits the strongest oscillations. This observation contradicts a potential origin of the oscillations from secondary electron transport because electrons from higher energy protons have larger ranges. Based on these observations we conclude that the small negative values of $K(x)$ of diode-type detectors are caused by a previously described artifact often observed in the iterative deconvolution process at sharp edges that is referred to as edge or ringing artifact (Xiong et al., 2011). Possible methods to suppress these artefacts in $K(x)$ of solid state detectors are to either introduce a negativity constraint or by a geometrical weighting function to compensate for volume averaging as suggested also for photon fields in TRS-483 (Palmans et al., 2017).

4.3 Influence of the incident proton energy and measurement depth

Both the spectral and scattering angle distributions of the primary and secondary particles are expected to change as a function of measurement depth and incident proton energy. In photon fields, the functions $K(x)$ have been shown to depend on the nominal photon energy due to the associated range of the secondary electrons, but can be considered depth independent for the same incident photon beam quality (Looe et al., 2017). Since volume-averaging was found to be the main contribution to the resulting volume effect in proton beams, the energy dependence of $K(x)$ is expected to be much smaller than in photon fields. In fact, the $K(x)$ functions derived in this work using three incident proton energies of 60 MeV, 150 MeV and 240 MeV were found to be very similar (compare figure 7 ((a) and (b))).

Therefore, the question arises whether it is sufficient to characterize the detector's volume effect in proton beams by using only one detector specific $K(x)$ determined at a single proton energy and depth, as was done experimentally in this study. This was investigated by considering profiles for various incident proton energies and measurement depths. For the former, $K_{150\mathrm{MeV}}(x)$ was convolved with the simulated $D_{60\mathrm{MeV}}(x)$ or $D_{240\mathrm{MeV}}(x)$ and compared to the simulated $M_{60\mathrm{MeV}}(x)$ or $M_{240\mathrm{MeV}}(x)$ (compare figure 8). For the latter, $K_{150\mathrm{MeV}}(x)$ determined at 2 cm depth was applied to larger measurement depths of 8 cm and 13 cm, where its applicability was studied by comparing the convolution products $K_{2\mathrm{cm}}(x) * D_{8\mathrm{cm}}(x)$ and $K_{2\mathrm{cm}}(x) * D_{13\mathrm{cm}}(x)$ with the actual measurements of $M_{8\mathrm{cm}}(x)$ or $M_{13\mathrm{cm}}(x)$, respectively (compare figure 4). In both cases, good agreement was found with a maximum difference of 0.06.

4.4 *K(x)* in the context of clinical proton dosimetry

The results from this study demonstrate that the volume-averaging within the extended sensitive detector volume dominates the volume effect in proton beams. For air-filled ionization chambers, the low-density air cavity is shown to cause further fluence perturbations. However, this is not the case for diode-type detectors, where both the semiconductor chips and other housing materials are not causing observable perturbation effects apart from the volume-averaging.

Furthermore, due to the broadening of the dose profile with increasing depth, the influence of the detector's volume effect also becomes less prominent at larger depths. This underlines the conclusion from previous studies that measurements of pencil beams or PBS treatment plans, which generally have relatively large penumbras, can be characterized correctly with the detectors studied in these works (Sahoo et al., 2010; Sawakuchi et al., 2010; Schwaab et al., 2011; Furukawa et al., 2013; Brodbek et al., 2020). Nevertheless, the selection of the detector used for profile measurements may be more important in the future as recent works have described attempts to reduce the penumbra in proton therapy (Hyer et al., 2014; Lomax, 2018; Winterhalter et al., 2018; Ciocca et al., 2019; Grevillot et al., 2020).

The results presented here show that such sharp penumbra fields cannot be measured accurately even when using small point-like ionization chambers unless the data are corrected for the spatial response of the detector. Currently such chambers are listed as suitable detectors for measuring scattered and scanned beam profiles in the Task group 224 report on proton therapy machine QA (Arjomandy et al., 2019) and were also recommended for measurements in dose gradients in a review of clinical dosimetry in scanned ion beam dosimetry (Giordanengo et al., 2017). Rath and Sahoo (2016) state that small-volume ionization chambers can be used for lateral profile measurements but point out that such measurements may need a correction for the detector size. The findings of this work can guide the choice of detectors for characterizing complex protons fields. In addition, the $K(x)$ determined in this work can be used in conjunction with the convolution model to derive field size dependent correction factors (Looe et al., 2015; Poppinga et al., 2015, 2018) or to recover the dose profiles from the detector signal profiles perturbed by the volume effect (Schwaab et al., 2011; Brodbek et al., 2020).

5 Conclusion

The volume effect of a detector perturbs the measurement process of small fields and lateral dose profiles. This perturbation can be characterized using the associated lateral dose response function $K(x,y)$ within the framework of an established convolution model. While $K(x)$ were investigated in various studies for photon fields, these functions are presented for the first time for proton beams for three ionization chambers, a diode and a diamond detector. Contrary to photon fields, the density perturbation caused by the non-water equivalent materials is small in proton beams and the volume-averaging from the extended sensitive volume is the main determinant of the volume effect. $K(x)$ determined at 150 MeV and 2 cm depth were used at different incident energies and depths to estimate potential errors. Considering the associated results, we could conclude that the $K(x)$ can be considered energy and depth independent, so that the $K(x)$ determined with an incident proton energy of 150 MeV and at a measurement depth of 2 cm in this work can be applied to describe the distortion of measured lateral profiles for all depth positions up to the Bragg-peak and for incident energies between 60 MeV and 240 MeV. For an exemplary gaussian shaped field with a sigma of 2 mm, the signal reduction at the field center as a result of the volume effect was calculated to be 17% smaller for protons compared to photons for a Semiflex 3D ionization chamber, whereas the measured output is 2% larger for protons than for photons when using a microDiamond detector. The determined $K(x)$ functions can be used to correct for volume effect perturbations and to derive small field correction factors that are especially important for measurements in small proton beams or collimated proton beams with sharp lateral dose profiles.

Acknowledgement

The authors thank PTW Freiburg and IBA Dosimetry for providing the detectors investigated in this study. Experiments were performed at the PARTREC Accelerator Facility of the University Medical Center Groningen, University of Groningen. Beam time was partly funded by the EU Horizon 2020 project ENSAR2 (contract no. 654002). Monte Carlo simulations were performed on the HPC Cluster CARL funded by the DFG under INST 184/157-1 FUGG.

References

Arjomandy, B., Taylor, P., Ainsley, C., Safai, S., Sahoo, N., Pankuch, M., Farr, J.B., Yong Park, S., Klein, E., Flanz, J., Yorke, E.D., Followill, D., Kase, Y., 2019. AAPM task group 224: Comprehensive proton therapy machine quality assurance. Med. Phys. 46. https://doi.org/10.1002/mp.13622

Brodbek, L., Kretschmer, J., Willborn, K., Meijers, A., Both, S., Langendijk, J.A., Knopf, A., Looe, H.K., Poppe, B., 2020. Analysis of the applicability of two-dimensional detector arrays in terms of sampling rate and detector size to verify scanned intensity-modulated proton therapy plans. Med. Phys. 47, 4589–4601. https://doi.org/10.1002/mp.14346

Ciocca, M., Magro, G., Mastella, E., Mairani, A., Mirandola, A., Molinelli, S., Russo, S., Vai, A., Fiore, M.R., Mosci, C., Valvo, F., Via, R., Baroni, G., Orecchia, R., 2019. Design and commissioning of the non-dedicated scanning proton beamline for ocular treatment at the synchrotron-based CNAO facility. Med. Phys. 46, 1852–1862. https://doi.org/10.1002/mp.13389

Delfs, B., Blum, I., Tekin, T., Schönfeld, A., Kranzer, R., Poppinga, D., Giesen, U., Langner, F., Kapsch, R., Poppe, B., Looe, H.K., 2021. The role of the construction and sensitive volume of compact ionization chambers on the magnetic field-dependent dose response. Med. Phys. 48, 4572–4585. https://doi.org/10.1002/mp.14994

Delfs, B., Poppinga, D., Ulrichs, A.-B., Kapsch, R.-P., Harder, D., Poppe, B., Looe, H.K., 2018. The 1D lateral dose response functions of photon-dosimetry detectors in magnetic fields—measurement and Monte-Carlo simulation. Phys. Med. Biol. 63, 195002. https://doi.org/10.1088/1361-6560/aadd3d

Francescon, P., Beddar, S., Satariano, N., Das, I.J., 2014. Variation of kQclin,Qmsrfclin,fmsr for the small-field dosimetric parameters percentage depth dose, tissue-maximum ratio, and off-axis ratio: Variation of kQclin,Qmsrfclin,fmsr for small-field dosimetric parameters. Med. Phys. 41, 101708. https://doi.org/10.1118/1.4895978
Furukawa, T., Inaniwa, T., Hara, Y., Mizushima, K., Shirai, T., Noda, K., 2013. Patient-specific QA and delivery verification of scanned ion beam at NIRS-HIMAC: QA and verification for scanning delivery. Med. Phys. 40, 121707. https://doi.org/10.1118/1.4828845
Gago-Arias, A., Brualla-González, L., González-Castaño, D.M., Gómez, F., García, M.S., Vega, V.L., Sueiro, J.M., Pardo-Montero, J., 2012. Evaluation of chamber response function influence on IMRT verification using 2D commercial detector arrays. Phys. Med. Biol. 57, 2005–2020. https://doi.org/10.1088/0031-9155/57/7/2005
Giordanengo, S., Manganaro, L., Vignati, A., 2017. Review of technologies and procedures of clinical dosimetry for scanned ion beam radiotherapy. Phys. Med. 43, 79–99. https://doi.org/10.1016/j.ejmp.2017.10.013
Grevillot, L., Osorio Moreno, J., Letellier, V., Dreindl, R., Elia, A., Fuchs, H., Carlino, A., Kragl, G., Palmans, H., Vatnitsky, S., Stock, M., 2020. Clinical implementation and commissioning of the MedAustron Particle Therapy Accelerator for non-isocentric scanned proton beam treatments. Med. Phys. 47, 380–392. https://doi.org/10.1002/mp.13928
Harder, D., Looe, H.K., Poppe, B., 2014. Convolutions and Deconvolutions in Radiation Dosimetry, in: Comprehensive Biomedical Physics. Elsevier, pp. 249–269. https://doi.org/10.1016/B978-0-444-53632-7.00913-8
Hoehr, C., Lindsay, C., Beaudry, J., Penner, C., Strgar, V., Lee, R., Duzenli, C., 2018. Characterization of the exradin W1 plastic scintillation detector for small field applications in proton therapy. Phys. Med. Biol. 63, 095016. https://doi.org/10.1088/1361-6560/aabd2d
Hyer, D.E., Hill, P.M., Wang, D., Smith, B.R., Flynn, R.T., 2014. A dynamic collimation system for penumbra reduction in spot-scanning proton therapy: Proof of concept: Penumbra trimmer for spot scanning. Med. Phys. 41, 091701. https://doi.org/10.1118/1.4837155
Kretschmer, J., Dulkys, A., Brodbek, L., Stelljes, T.S., Looe, H.K., Poppe, B., 2020. Monte Carlo simulated beam quality and perturbation correction factors for ionization chambers in monoenergetic proton beams. Med. Phys. 47, 5890–5905. https://doi.org/10.1002/mp.14499
Laub, W.U., Wong, T., 2003. The volume effect of detectors in the dosimetry of small fields used in IMRT. Med. Phys. 30, 341–347. https://doi.org/10.1118/1.1544678
Lomax, A., 2018. What will the medical physics of proton therapy look like 10 yr from now? A personal view. Med. Phys. 45. https://doi.org/10.1002/mp.13206
Looe, H.K., Harder, D., Poppe, B., 2017. The energy dependence of the lateral dose response functions of detectors with various densities in photon-beam dosimetry. Phys. Med. Biol. 62, N32–N44. https://doi.org/10.1088/1361-6560/aa54aa
Looe, H.K., Harder, D., Poppe, B., 2015. Understanding the lateral dose response functions of high-resolution photon detectors by reverse Monte Carlo and deconvolution analysis. Phys. Med. Biol. 60, 6585–6607. https://doi.org/10.1088/0031-9155/60/16/6585
Looe, H.K., Stelljes, T.S., Foschepoth, S., Harder, D., Willborn, K., Poppe, B., 2013. The dose response functions of ionization chambers in photon dosimetry – Gaussian or non-Gaussian? Z. Für Med. Phys. 23, 129–143. https://doi.org/10.1016/j.zemedi.2012.12.010

MATLAB, 2019. version 9.7.0.1190202 (R2019b). The MathWorks Inc., Natick, Massachusetts.
McAuley, G.A., Teran, A.V., Slater, J.D., Slater, J.M., Wroe, A.J., 2015. Evaluation of the dosimetric properties of a diode detector for small field proton radiosurgery. J. Appl. Clin. Med. Phys. 16, 51–64. https://doi.org/10.1120/jacmp.v16i6.5391
Moignier, C., Tromson, D., de Marzi, L., Marsolat, F., García Hernández, J.C., Agelou, M., Pomorski, M., Woo, R., Bourbotte, J.-M., Moignau, F., Lazaro, D., Mazal, A., 2017. Development of a synthetic single crystal diamond dosimeter for dose measurement of clinical proton beams. Phys. Med. Biol. 62, 5417–5439. https://doi.org/10.1088/1361-6560/aa70cf
Mulder, J., 2017. Water calorimetry for proton therapy: implementing a primary dose measurement standard (PhD-thesis). University of Groningen.
Palmans, H., Andreo, P., Huq, M.S., Seuntjens, J., International Atomic Energy Agency, American Association of Physicists in Medicine, 2017. Dosimetry of small static fields used in external beam radiotherapy: an international code of practice for reference and relative dose determination.
Poppinga, D., Delfs, B., Meyners, J., Harder, D., Poppe, B., Looe, H.K., 2018. The output factor correction as function of the photon beam field size – direct measurement and calculation from the lateral dose response functions of gas-filled and solid detectors. Z. Für Med. Phys. 28, 224–235. https://doi.org/10.1016/j.zemedi.2017.07.006
Poppinga, D., Meyners, J., Delfs, B., Muru, A., Harder, D., Poppe, B., Looe, H., 2015. Experimental determination of the lateral dose response functions of detectors to be applied in the measurement of narrow photon-beam dose profiles. Phys. Med. Biol. 60, 9421–9436. https://doi.org/10.1088/0031-9155/60/24/9421
Rath, A.K., Sahoo, N. (Eds.), 2016. Particle Radiotherapy. Springer India, New Delhi. https://doi.org/10.1007/978-81-322-2622-2
Sahoo, N., Ciangaru, G., Sawakuchi, G., Anand, A., Poenisch, F., Suzuki, K., Mohan, R., Gillin, M., Zhu, X., 2010. SU-GG-T-463: Study of the Magnitude of Detector Size Effect in the Measured Lateral Profiles of Proton Pencil Beam Spots. Med. Phys. 37, 3293–3293. https://doi.org/10.1118/1.3468861
Sawakuchi, G.O., Zhu, X.R., Poenisch, F., Suzuki, K., Ciangaru, G., Titt, U., Anand, A., Mohan, R., Gillin, M.T., Sahoo, N., 2010. Experimental characterization of the low-dose envelope of spot scanning proton beams. Phys. Med. Biol. 55, 3467–3478. https://doi.org/10.1088/0031-9155/55/12/013
Schwaab, J., Brons, S., Fieres, J., Parodi, K., 2011. Experimental characterization of lateral profiles of scanned proton and carbon ion pencil beams for improved beam models in ion therapy treatment planning. Phys. Med. Biol. 56, 7813–7827. https://doi.org/10.1088/0031-9155/56/24/009
Sechopoulos, I., Rogers, D.W.O., Bazalova-Carter, M., Bolch, W.E., Heath, E.C., McNitt-Gray, M.F., Sempau, J., Williamson, J.F., 2018. RECORDS: improved Reporting of montE CarlO RaDiation transport Studies: Report of the AAPM Research Committee Task Group 268. Med. Phys. 45, e1–e5. https://doi.org/10.1002/mp.12702
Seltzer, S.M., Fernández-Varea, J.M., Andreo, P., Bergstrom, P.M., Burns, D.T., Krajear Bronié, I., Ross, C.K., Salvat, F., 2016. Key data for ionizing radiation dosimetry: measurement standards and applications. ICRU Report 90. J. ICRU 14, 1–110.
Simiele, E., DeWerd, L., 2018. On the accuracy and efficiency of condensed history transport in magnetic fields in GEANT4. Phys. Med. Biol. 63, 235012. https://doi.org/10.1088/1361-6560/aaedc9

Tekin, T., Blum, I., Delfs, B., Schönfeld, A., Kapsch, R., Poppe, B., Looe, H.K., 2020. The dose response of high-resolution diode-type detectors and the role of their structural components in strong magnetic field. Med. Phys. 47, 6509–6518. https://doi.org/10.1002/mp.14535

Tekin, T., Blum, I., Delfs, B., Schönfeld, A.-B., Poppe, B., Looe, H.K., 2022. The magnetic field dependent displacement effect and its correction in reference and relative dosimetry. Phys. Med. Biol. 67, 045004. https://doi.org/10.1088/1361-6560/ac4a41

van Cittert, P.H., 1931. Zum Einfluß der Spaltbreite auf die Intensitätsverteilung in Spektrallinien. II. Z. Für Phys. 69, 298–308. https://doi.org/10.1007/BF01391351

Winterhalter, C., Lomax, A., Oxley, D., Weber, D.C., Safai, S., 2018. A study of lateral fall-off (penumbra) optimisation for pencil beam scanning (PBS) proton therapy. Phys Med Biol 15.

Wulff, J., Baumann, K.-S., Verbeek, N., Bäumer, C., Timmermann, B., Zink, K., 2018. TOPAS/Geant4 configuration for ionization chamber calculations in proton beams. Phys. Med. Biol. 63, 115013. https://doi.org/10.1088/1361-6560/aac30e

Xiong, R., Ding, W., Ma, S., Gao, W., 2011. A new image deblurring algorithm with less ringing artifacts via error variance estimation and soft decision, in: 2011 18th IEEE International Conference on Image Processing. Presented at the 2011 18th IEEE International Conference on Image Processing (ICIP 2011), IEEE, Brussels, Belgium, pp. 701–704. https://doi.org/10.1109/ICIP.2011.6116650